One Year Water Stable and Porous Bi(III) Halide Semiconductor with Broad Spectrum Antibacterial Performance

Ali Azmy,[1,#] Xue Zhao,[1,#] Giasemi K. Angeli,[2] Claire Welton,[4] Parth Raval,[4] Lukasz Wojtas,[1] Nourdine Zibouche,[3] G. N. Manjunatha Reddy,[4] Pantelis N. Trikalitis,[2] Jianfeng Cai,[1] and Ioannis Spanopoulos*[,1]

[1]*Department of Chemistry, University of South Florida, Tampa, Florida 33620, United States*
[2]*Department of Chemistry, University of Crete, 71003 Heraklion, Greece*
[3]*Department of Chemistry, University of Bath, Bath BA2 7AY, U.K.*
[4]*Univ. Lille, CNRS, Centrale Lille Institut, Univ. Artois, UMR8181-UCCS-Unité de Catalyse et Chimie du Solide, F-59000 Lille, France.*

ABSTRACT

Hybrid metal halide semiconductors pose as a unique family of materials with immense potential for numerous applications. For this to be materialized, environmental stability and toxicity deficiencies must be simultaneously addressed. We report here a porous, visible light semiconductor, namely (DHS)Bi_2I_8 (DHS = [2.2.2] cryptand), which consists of nontoxic, earth-abundant elements, and is water stable for more than a year. Gas and vapor-sorption studies revealed that it can selectively and reversibly adsorb H_2O and D_2O at room temperature (RT) while impervious to N_2 and CO_2. Solid-state NMR measurements and DFT calculations verified the incorporation of H_2O and D_2O in the molecular cages, validating its porous nature. In addition to porosity, the material exhibits broad band-edge light emission centered at 600 nm with a full width at half-maximum (FWHM) of 99 nm, which is maintained after six months of immersion in H_2O. Moreover, (DHS)Bi_2I_8 exhibits bacteriocidal action against three Gram-positive and three Gram-negative bacteria, including antibiotic-resistant strains. This performance, coupled with the recorded water stability and porous nature, renders it suitable for a plethora of applications, from solid-state batteries to water purification and disinfection.

Keywords: water stability, porous semiconductors, metal halides, antibacterial activity, water adsorption, gas selectivity

INTRODUCTION

Hybrid halide perovskite semiconductors with general formula AMX_3 (A = $CH_3NH_3^+$ (MA), $HC(NH_2)_2^+$ (FA), Cs^+; M = Ge^{2+}, Sn^{2+}, Pb^{2+}; X = Cl^-, Br^-, I^-)[1,2], have proven to be prominent candidates for many applications, spanning from solar cells[3-4] and LEDs[5-6] to photodetection,[7] thermography,[8] photocatalysis[9] and lasing.[10] Their organic-inorganic nature offers multiple nodes for tuning not only the optoelectronic[11-13] but also the mechanical properties of the corresponding compounds.[14-15] Despite advances in materials engineering pertaining to the use of elaborate organic counter-cations that render these semiconductors air and water stable, a permanent solution remains elusive.[16-19] Towards this end, we recently developed a strategy that gave rise to metal halide semiconductors with record water stability (more than a year) using molecular cages acting as structure-directing agents and counter-cations. The corresponding material belongs to a new family of materials, namely porous metal halide semiconductors (PMHS).[20] Long-term environmental stability will bring hybrid halide semiconductors not only a step closer to commercialization[21] but render them proper for new applications beyond optoelectronics.

Of particular interest is the evaluation of metal halide materials as antibacterial agents, an emerging and quite impactful application.[22] Apparently, hybrid metal complexes offer significant advantages over fully organic or fully inorganic compounds.[23-24] Antimicrobial Resistance (AMR) is identified by the World Health Organization (WHO) as one of the greatest threats humanity faces, and this problem is expected to deteriorate over the following decades.[25-26] Despite advances in antibiotics development, the rapid rates at which bacteria develop resistance are alarming. Therefore, there is immense interest in the scientific community in developing next-generation drug candidates with improved antibacterial efficiency, efficacy, and selectivity.[27-29]

Current commercially available antibacterial compounds are based on either organic molecules (e.g. nitrofurazone (NZF)[30] and ampicillin[31] targeting E.coli, nitrofurantoin (NFT)[32] targeting MRSA, and argyrin[33] targeting P. aeruginosa) or inorganic complexes (e.g. silver (Ag(I))[34] and bismuth (Bi(III) compounds).[35] Bacteria are quite competent in adopting mechanisms for degrading organic antibacterial agents[36]. At the same time, inorganic and hybrid candidate materials have proven to be more versatile having access to unique modes of action.[37-39] In particular, these pertain to ligand exchange or release,[40] generation of reactive oxygen species (ROS),[41] redox

activation[42], and catalytic generation of toxic species or depletion of essential substrates.[43] Such mechanisms are difficult, if not impossible, to replicate with purely organic compounds.[44-45]

Nonetheless, metallodrugs share toxicity, bioaccumulation, and long-term in vivo stability deficiencies.[46-47] Among the most widely utilized metallodrugs are the Ag(I) based compounds, such as silver sulphadiazine (Silvadene, Silverex, Silvazine, SSD, Thermazene), which are applied as a cream formulation to prevent and treat infections.[48] However, the toxicity and bioaccumulation of Ag(I) limits its broad use as a metallodrug. Bi(III), on the other hand, poses as an excellent metallodrug candidate due to its limited toxicity and biocompatibility.[49-51] Currently, commercially available Bi(III) metallodrugs such as colloidal bismuth subcitrate (CBS, DeNol) or ranitidine bismuth citrate (RBC, Pylorid, Tritec) are used to treat peptic ulcers that are often associated with *Helicobacter pylori* (*H. pylori)*.[52-53]

Notably, bismuth metal halides emerged recently as promising antibacterial candidates. Ouerghi et al. reported that $(C_6H_7NCl)_3[BiCl_6]\cdot H_2O$ exhibits antimicrobial activity against *Pseudomonas aeruginosa (P. aeruginosa), Escherichia coli* (*E. coli*), *Salmonella typhimurium*, and methicillin-resistant *Staphylococcus aureus* (MRSA).[54] Ali et al., found that $(C_{12}H_{14}N_2O_2S)_2[Bi_4I_{16}]\cdot 4H_2O$ exhibited antioxidant and antibacterial activity against *E.coli*, *Listeria monocytogenes*, *Salmonella enterica*, MRSA, *Micrococcusluteus, Bacillus cereus, Enterobacter aeruginosa,* and *P. aeruginosa*.[55] Aygun et al. synthesized a series of bismuth(III) halides with benzaldehyde-N1-alkyl-thiosemicarbazone that were found to be most active against *E.coli*.[56] Ozturk et al., demonstrated that bismuth(III) thiosemicarbazone complexes, such as $BiCl_3(\eta^1\text{-S-Hacptsc})_3$ (Hacptsc = acetophenone thiosemicarbazone), exhibited toxicity against MCF-7 and MRC-5 cells, and antibacterial activity against *E.coli* and *P. aeruginosa*.[57] Turk et al., reported a series of bismuth(III) halide thiosemicarbazone complexes, such as $BiCl_2(\mu_2\text{-Cl})(\eta1\text{-S-Httsc})_2]_2$ and $[BiI_2(\mu_2\text{-I})(\eta1\text{-S-Httsc})_2]_2$, (Httsc: thiophene-2-carbaldehyde thiosemicarbazone), that exhibited activity against MCF-7 cells, and antibacterial activity against *E.coli*, MRSA and *P. aeruginosa*.[58] Scaccaglia et al. assembled a series of complexes with general formula $BiLCl_2$ (L is a quinoline thiosemicarbazone) with bactericidal activity against *Klebsiella pneumonia (K. pneumonia)*.[59]

Despite their performance, the vast majority of the reported compounds do not exhibit water stability. This trait can hinder their broad utilization in applications

beyond therapeutics, from water purification and disinfection,[60] personal protective equipment (PPE) antibacterial coatings,[61] antibacterial coatings in respirators,[62] to food packaging applications.[63]

Addressing these concerns, we utilized a novel synthetic strategy developed recently by our group to generate water-stable metal halide materials by using porous molecular cages. Reaction of [2.2.2] cryptand (DHS) with Bi(III) gave rise to a 0D porous metal halide material. The corresponding compound (DHS)Bi_2I_8 is water stable for a year, while gas sorption studies demonstrated that it can selectively adsorb and desorb H_2O at RT, while it is impermeable to N_2, and CO_2. Furthermore, solid state ^1H and ^2H-NMR studies validated the H_2O inclusion in the DHS cavity. In addition to porosity, the corresponding metal halide is a direct bandgap semiconductor exhibiting band-edge PL emission at RT. The semiconducting nature has proven to be the reason behind the antibacterial performance of fully inorganic compounds such as TiO_2, $SrTiO_3$ and ZnO. Therefore a Bi(III) semiconductor poses as an excellent metallodrug candidate exhibiting multiple beneficent features. To validate our hypothesis, we evaluated the in vitro antimicrobial activity against three Gram-positive and three Gram-negative bacteria. Apparently, (DHS)Bi_2I_8 exhibits bacteriocidal action against *E. coli*, MRSA, methicillin-resistant *Staphylococcus epidermidis* (MRSE), vancomycin-resistant *Enterococcus faecium* (VREF), *K. pneumonia* and *P. aeruginosa*. Fluorescence microscopy and TEM studies shed light on the underlying mechanism, revealing that the bacteria cell membrane raptures in the presence of (DHS)Bi_2I_8. The broad range antimicrobial activity for both Gram-positive and Gram-negative bacteria, coupled with its unparallel water stability, render this visible light semiconductor a versatile antibacterial agent with potential use in a plethora of every day preventive care applications.

EXPERIMENTAL SECTION

Starting Materials and Bacteria Strains

All starting materials for synthesis were purchased commercially and were used without further purification. Bismuth(III) oxide, 98+%, pure was purchased from Acros Organics, Hydriodic acid 57 wt. % in H_2O, distilled, stabilized, 99.95%, Hypophosphorous acid solution 50 wt. % in H_2O were purchased from Aldrich and 4,7,13,16,21,24-Hexaoxa-1,10-diazabicyclo[8.8.8]hexacosane (DHS) was purchased from AmBeed. Tryptic Soy Broth (TSB), 4′,6-diamidino-2-phenylindole (DAPI) and propidium iodide (PI) were obtained from Sigma-Aldrich. The antibacterial activity of the material was evaluated by using Gram-positive MRSA (ATCC 33591), MRSE (RP62A), VREF (ATCC700802) and Gram-negative E. coli (ATCC 25922), *K. pneumonia* (ATCC 13383), and *P. aeruginosa* (ATCC 27853).

Material Synthesis

(DHS)Bi_2I_8: 95 mg (0.25 mmol) of DHS linker were dissolved in a solution consisting of 2 mL of 57 wt. % HI and 0.5 ml 50 wt. % H_3PO_2, by heating under constant magnetic stirring. Then 233 mg (0.5 mmol) of Bi_2O_3 were added to the hot colorless solution. Heating was discontinued and the sample was left to cool to RT directly. Dark orange crystals deposited after 10 min. They were collected by suction filtration and dried under vacuum overnight.

Bacterial Inhibition Study

Gram-negative bacterial (*E. coli*, *K. pneumonia*, and *P. aeruginosa*) and Gram-positive bacterial including (MRSA, MRSE and VREF) were grown in Tryptic Soy Broth (TSB) medium at 37 °C for 16 h. Then the bacterial were incubated until mid-log phase by transferring 100 μL of the bacterial solution to 4 mL of fresh TSB medium and shaking at 37 °C for 6 h. 50 μL of bacteria at a concentration of 10^6 CFU/mL was added into centrifuge tubes with no material, 1 mg and 10 mg of material respectively, which was followed by adding 50 μL of fresh TSB medium in each tube. The mixture was incubated at 37 °C for 16 h and 100 μL of supernatant was transferred into 96-well plate. The plate was investigated, imaged and OD_{600} value was measured by BioTek multimode microplate reader Synergy H4 to study bacterial inhibition.

Standard Plate Counting Assay

MRSA was cultured in TSB medium at 37 °C for 16 h plus 6 h to achieve mid-log phase and then diluted to get bacterial solution at concentration of 10^6 CFU/mL. 50 μL of bacteria was added into Eppendorf tubes with no material, 1 mg and 10 mg of material respectively, which was followed by adding 50 μL of fresh TSB medium in each tube. After incubated at 37 °C for 16 h, the mixture was diluted properly and grown in TSB agar plate, followed by incubation at 37 °C for 12 h or 24 h. The MRSA colonies were observed and counted respectively.

Fluorescence Microscopy Imaging

After MRSA was incubated into mid-log phase in TSB medium, the bacterial solution was diluted by 100-fold with fresh medium to obtain 10 mg/mL of material in 3 mL of bacterial solution in total. The solution was treated with no bacterial as negative control. The mixture was incubated at 37 °C for 4 h and the bacterial solution without solid material was centrifuged at 3000 rpm at 4 °C for 10 min to collect cells. The cell pellets were washed with 1× PBS buffer for three times, then incubated with 5 μg/mL of PI and 10 μg/mL of DAPI sequentially on ice for 15 min in dark. Then the stained cells were washed with 1 × PBS for three times and suspended by 100 μL of 1 × PBS buffer. The slides were prepared by addition of 10 μL of bacterial solution and fixation with cold methanal. It was observed and imaged under Olympus FV1000 MPE Multiphoton Laser Scanning Microscope.

TEM studies

MRSA was grown into mid-log phase and the bacterial solution was diluted by 100-fold to 3 mL of fresh TSB medium with 10 mg/mL of material. After incubation at 37 °C for 4 h and removal of solid material, the bacterial pellets were collected by centrifuging at 3000 rpm at 4 °C for 15 min. The cells untreated with material was considered as negative control. After washed by 1 × PBS for three times, the concentrated cells were resuspended by 100 μL of deionized water. Then 10 μL of bacterial samples were dropped on the surface of TEM grids and dried in vacuum at 45 °C for 30 s. TEM images were obtained using an FEI Morgagni 268D TEM operated at 60 kV with an Olympus MegaView III camera.

Solid state NMR measurements

Polycrystalline materials were used to acquired solid-state NMR spectra. These materials were separately packed into 1.3 mm (outer diameter) zirconia rotors fitted with VESPEL® caps. For moisture exposure experiments, samples were placed into different hydration chambers containing water and water-d vapor at 85% relative humidity (RH) in the air. Samples were taken out from the humidity chamber at different intervals, and *ex-situ* solid-state ^1H and ^2H MAS NMR experiments were carried out. All solid-state MAS NMR experiments were carried out using a 18.8 T (^1H, 800.1 MHz) Bruker AVANCE NEO NMR spectrometer with a 1.3 mm H-X probehead. Unless otherwise specified, all samples were spun at 50 kHz magic-angle spinning (MAS) frequency. The ^1H relaxation delays were determined from saturation recovery measurements and analyses. All ^1H

MAS NMR spectra were acquired by coaddition of 16 transients. All ^{2}H MAS NMR spectra were acquired by coaddition of 1024 transients. The ^{1}H experimental shift was calibrated with respect to neat TMS using adamantane as an external reference (^{1}H resonance, 1.82 ppm). For ^{2}H MAS spectra, the chemical shifts are calibrated with respect to TMS using liquid D_2O as an external reference (^{2}H resonance, 4.80 ppm)**.**

XRD measurements

Single-crystal X-ray diffraction

X-ray diffraction data were measured on a Bruker D8 Venture PHOTON II CMOS diffractometer equipped with a Cu Kα INCOATEC ImuS micro-focus source (λ = 1.54178 Å) equipped with a cryostream 800 system (Oxford Cryosystems) for temperature regulation. Indexing was performed using APEX4 (Difference Vectors method).[64] Data integration and reduction were performed using SaintPlus.[65] Absorption correction was performed by multi-scan method implemented in SADABS.[66] Space group was determined using XPREP implemented in APEX3. Structure was solved using SHELXT[67] and refined using SHELXL-2018/3 (full-matrix least-squares on F2)[68] through OLEX2 interface program.[69] Ellipsoid plot was done with Platon.[70] Disordered molecule was refined with restraints. All hydrogen atoms were located geometrically and were refined using riding model.

Powder X-ray diffraction

Powder X-ray diffraction patterns were collected on a Bruker D8 Advance Diffractometer with Lynxeye detector using CuKα radiation. X-ray source operated at 40kV/40mA and Ni filter was used to suppress Kbeta radiation. 2.5 deg primary and secondary Soller slits were used to suppress axial divergence. Diffraction patterns were recorded from 2 to 60 2θ in variable slits mode and with knife edge installed. A typical scan rate was 20 sec/step with a step size of 0.02 deg.

Variable Temperature high resolution Powder X-ray diffraction

High resolution variable Temperature Powder X-ray diffraction measurements were performed at APS Argonne National Lab, on beamline 11BM, with an average wavelength of 0.458955 Å. Discrete detectors covering an angular range from 0 to 4 2θ were scanned over a 28 2θ range, and data points were collected e very 0.001 2θ at a scan speed of 0.1/s. The data were manipulated with CMPR,[71] and Rietveld analysis was performed using Bruker Topas 5 Software.

Optical Spectroscopy

Optical diffuse-reflectance measurements were performed at room temperature using a Cary 5000 UV-Vis-NIR Spectrophotometer, coupled with an integrating sphere, from 200 to 2500 nm. $BaSO_4$ was used as a non-absorbing reflectance reference. The generated reflectance-versus-wavelength data were used to estimate the band gap of the material by converting reflectance to absorbance data according to the Kubelka−Munk equation: $\alpha/S = (1 - R)^2/2R$, where R is the reflectance and α and S are the absorption and scattering coefficients, respectively.[72]

PL/PLE/TRPL measurements

PL, PLE and TRPL studies were performed using an Edinburgh Instruments FS5 Spectrofluorometer equipped with a 150 W xenon lamp and a 470 nm EPL picosecond pulsed diode laser.

TGA-DSC measurements

Thermogravimetric Analysis (TGA) measurements were performed on a TA Instruments Q50 Thermogravimetric Analyzer. An amount of ~23 mg of sample was placed inside an Alumina Pan and heated up to 700 ^{o}C under N_2 flow with a heating rate of 3 ^{o}C/min. Differential Scanning Calorimetry (DSC) measurements were performed on a TA Instruments Q20 Differential Scanning Calorimeter. An amount of 4 mg of sample was placed inside an Aluminium Pan and heated up to 250 ^{o}C under N_2 flow with a heating rate of 10 ^{o}C/min.

SEM/EDS

Scanning Electron Microscopy (SEM) measurements were recorded on a high-resolution thermal field emission source Hitachi SU-70. Data were acquired with an accelerating voltage of 25 kV. The

EDS was performed with a Hitachi s-800 FESEM using a EDAX SDD detector. The samples were prepared by pressing the powder on to a substrate of carbon adhesive tape and tilting the sample to 30 degrees. The electron beam energy was set to 21 KeV with a beam current of 1 nA for quantification.

Gas-sorption measurements. Gas sorption measurements for N_2 and CO_2 were recorded at 77 K and 195 K respectively up to 1 bar, using a state-of-the-art, high precision BELSORP-maxII from Microtrac MRB, equipped with four (4) analysis stations and a detachable thermostatic bath for accurate measurements. For the aforementioned measurements the desired cryogenic temperature was achieved using a bath of liquid nitrogen (LN_2, 77 K, N_2) and a mixture of acetone/dry ice (195 K, CO_2) in a cryogenic dewar as a coolant. The bright red powder sample was placed in a 9 mm pre-weighted quartz cell and then it was activated *in situ* using a 4-position heater, at 100 ^oC for 10 hours, under ultrahigh vacuum ($<1x10^{-5}$ Pa). After the activation process the cell was re-weighted to measure the exact mass (0.0641 g) of the sample and then it was placed at the analysis station.

Vapor-sorption measurements. Vapor sorption isotherms for H_2O, and D_2O were recorded at 298 K up to 1 bar, using the same apparatus. The desired temperature was achieved with the use of the detachable thermostatic bath. The material was re-activated following the procedure described above. Prior to measurements, each vapor was degassed to remove any dissolved gases following a standard protocol. For comparison purposes, all isotherms are presented as the amount adsorbed as a function of the relative pressure, p/p_0, where p_0 is the saturation pressure of the vapor at the measurement temperature.

DFT Studies

We carried out density functional theory (DFT) calculations as implemented in the Quantum ESPRESSO package.[73-74] For the reaction energies, the Kohn-Sham wave-functions and energies are calculated with the GGA-PBE[75-76] for electron exchange and correlation, using a plane-wave basis, with energy and charge density cutoffs of 40 and 400 Ry, respectively. The Grimme dispersion correction DFT-D3,[77-78] was used to account for the dispersion corrections. Ultrasoft pseudopotentials are used to describe the core-valence interactions.[79] The structural relaxation is performed until the force on each atom is smaller than 0.01 eV/Å. For the geometry optimization, a *k*-point sampling of 6x3x6 was used for the Brillouin zone integration and a 8x8x2 k-mesh for the electronic structure analysis following the Monkhorst-Pack scheme.[80] The pristine system contains of 296 atoms. We have included water molecules inside the linkers assess the material's stability.

RESULTS AND DISCUSSION

Synthetic aspects and structural characterization

High-quality, dark orange plate single crystals of (DHS)Bi_2I_8 can be acquired through the reaction of Bi(III) oxide and the DHS linker in a hot HI solution (Figure S1. Single crystal X-ray diffraction (XRD) studies revealed a 0D structure that crystallizes in the monoclinic space group $P2_1/c$ (Figure 1 and Table 1). It consists of tetramers of edge-sharing $[BiI_6]^{3-}$ octahedra that are separated and charged balanced by the DHS ligands. The overall connectivity of the centrosymmetric tetranuclear anion can be described as a pair of edge-sharing bi-octahedra, which mutually share two and three cis edges respectively (Figure 1c). There are two crystallographically independent Bi atoms and eight I atoms that constitute the two octahedra of the tetramers, while adjacent tetramers lay at a distance of 4.2 Å.

The Bi-I bond lengths fall into two groups. One in the short range, spanning from 2.9036(14) Å to 2.9349(17) Å, recorded for the non-bridging iodide atoms and one in the long-range, spanning from 3.0501(13) Å to 3.3457(15) Å, for the bridging iodide atoms (Table S3). These values correlate well with other iodobismuthates(III) consisting of $[BiI_6]^{3-}$ octahedra such as (4AMP)BiI_5 and $Rb_3Bi_2I_9$.[81-82] There is a slight distortion of the corresponding octahedra, evident by the I-Bi-I angles that range from 83.80(3)° to 164.67(4)° for the cis and trans arrangements respectively (Table S4). This gives rise to bond angle variance values of 37.65 deg.^{2} and 18.34 deg.^{2} for $[Bi(2)I_6]^{3-}$ and $[Bi(1)I_6]^{3-}$ octahedra. Interestingly, the corresponding tetramer is the same as in the case of $(C_{12}H_{14}N_2O_2S)_2[Bi_4I_{16}]\cdot 4H_2O$ compound.[55] Notably, Bi-I bond lengths and I-Bi-I angles closely match the two materials.

The organic counter-cations are eclipsed along the *a* axis, laying at a distance of 2.7 Å, revealing a hexagonal arrangement motif, templated by the protruding axial iodide atoms of the tetramer (Figure 1a). Interestingly, there is approximately one crystalline H_2O present per three DHS ligands. It is located in close vicinity of DHS and hydrogen bonded to its oxygen atoms. Hydrated DHS appears to have slightly different conformation, leading to a small disorder. For simplicity purposes, the dehydrated formula will be utilized throughout the text.

In-house powder X-ray diffraction studies (PXRD) verified the uniform phase purity of the corresponding materials as the experimental and calculated patterns from single crystal XRD studies are identical (Figures 2 and S2). Energy-dispersive X-ray

spectroscopy (EDS) studies confirmed the (DHS)Bi_2I_8 formula, revealing a Bi:I ratio of 1:4 (Figure S3).

To shed light on the thermal stability of the corresponding material, we performed high-resolution variable-temperature PXRD measurements using synchrotron radiation (APS-11BM). Apparently, there are no structural phase transitions from 100 K to 340 K, as the only difference among the recorded PXRD patterns is the gradual increase of the unit cell dimensions due to thermal expansion, as it is evident for the shift of the diffraction peaks to lower Q values (Figure 3). This is typical behavior for hybrid perovskites and metal halide materials.[83-84] The material maintains its structural integrity up to 340 K. At the same time, at 400 K, there is a significant broadening of the peaks and appearance of additional diffraction peaks at 0.6 Q, indicative of structural degradation. Thermogravimetric (TGA) analysis demonstrated that the material loses its crystalline H_2O at 90-120 °C, while the structure is thermally stable up to 285 °C, where a sharp weight loss appears.[85] There are two decomposition steps at ~285 °C and ~350 °C (Figure S4a). The first weight loss corresponds to the decomposition of the organic part of the structure and HI; the second step corresponds to the sublimation of BiI_3, in perfect agreement with previous studies.[86] Similar thermal stability performance has been recorded for Bi(III) perovskite materials.[81] Differential scanning calorimetry (DSC) measurements support the PXRD studies on the absence of phase transitions in the examined temperature range (25 – 250 °C) and further verify the loss of crystalline H_2O at ~101 °C (Figure S4b).

Fresh as made crystals were immersed in liquid water for 12 months without structural damage, as revealed by comparing the PXRD patterns from the fresh and water-aged crystals (Figure 2). This stability performance is the same as the other DHS-based semiconductor, $(DHS)_2Pb_5Br_{14}$, reported recently by our group.[20] To the best of our knowledge, this is record stability for hybrid Bi(III) metal halide semiconductors.[87-93]

Gas sorption studies

Despite the zero-dimensional nature of (DHS)Bi_2I_8 the presence of DHS cryptand offers a potential accessible space, as we recently demonstrated in the case of the porous 2D $(DHS)_2Pb_5Br_{14}$ material.[20] N_2 and CO_2 adsorption isotherms recorded at 77 K and 195 K in a previously activated solid at 100 °C under high vacuum reveal no sorption (Figure 4b). Remarkably and in marked contrast, H_2O and D_2O isotherms

recorded at 298 K show a type-I curve at low relative pressure (<0.15 p/p_o), followed by a gradual increase in uptake up to ~0.8 p/p_o and more pronounced adsorption between 0.8-0.95 p/p_o associated with condensation in interparticle meso- and macro-porosity (Figure 4a). The striking feature is the observed knee in the isotherm (type-I isotherm) at the low relative pressure (Figure 4a inset), indicating the presence of microporosity which is accessible by H_2O (2.65 Å) and D_2O but not with N_2 (3.64 Å) or CO_2 (3.30 Å), apparently due to the small kinetic diameter of the former (values in parentheses).[94] Notably, the H_2O uptake at ~0.1 p/p_o (Figure S5), just after the knee in the isotherm and in the valid range of relative pressures where micropores are completely filled, is ~0.4 mmol $g^{-1,}$ which is very close to the value 0.55 mmol g^{-1} calculated from the molecular formula of $(DHS)Bi_2I_8$, assuming one H_2O molecule per DHS cavity.

The results demonstrate that the available space offered by DHS counterions is accessible by H_2O and D_2O in the 0D $(DHS)Bi_2I_8$ solid, as in the case of the 2D $(DHS)_2Pb_5Br_{14}$ material, however in marked contrast, the adsorption process filling the small micropores are very different between the two cases. In particular, the 2D $(DHS)_2Pb_5Br_{14}$ solid shows a gradual increase in H_2O uptake (no knee) associated with slow adsorption kinetics, whereas for the 0D $(DHS)Bi_2I_8$ material, the observed type-I (knee) isotherm suggests a more facile process. The latter could be associated with the 0D nature of the material, presumably allowing the DHS molecules to respond more freely upon adsorption of H_2O, due to their flexible nature (sp^3-carbon atoms in DHS). On the contrary, the more rigid 2D materials limit the flexibility of DHS counterions that are confined between the inorganic layers of the structure. Therefore, $(DHS)Bi_2I_8$ represents the first example of a porous 0D semiconducting material originating from the presence of DHS molecules but with distinct behavior from the 2D $(DHS)_2Pb_5Br_{14}$ solid. These results demonstrate a unique and unprecedented synergy between the inorganic and organic parts in these hybrid solids offering novel opportunities in advanced materials design.

It is pointed out that the selective adsorption of H_2O over N_2 and CO_2 has been demonstrated before for ultramicoporous MOFs, such as MOF-802.[95]

Elucidation of short-range structures and interactions through solid-state (ss-) NMR spectroscopy.

ss-NMR was selected as a valuable method to illuminate the local structural environment of the adsorbed vapor molecules. Figure 5 presents ^{1}H and ^{2}H magic-angle spinning NMR spectra of (DHS)Bi_2I_8 before and after exposure to moisture at 85% relative humidity in the air. For the fresh material, the ^{1}H resonances corresponding to the -OCH_2 (3.8 ppm) and -NCH_2 (6.8 ppm) groups of cryptand were resolved and identified. By comparison, ^{1}H-MAS NMR spectrum of neat cryptand acquired under the same experimental conditions showed much border signals (Figure S6).[20] It indicates that the cryptands molecules brought into the porous material lead to highly ordered networks, whereby the local changes in the non-covalent packing interactions between cryptand molecules and bismuth iodide octahedra are expected to contribute to the ^{1}H-NMR lineshape. It is further corroborated by analysing ^{1}H and ^{2}H-NMR spectra of the same material acquired after exposure to moisture at 85% relative humidity (RH) in the air.[96-97] In moisture aged (1h, 85% RH in D_2O/H_2O vapor) sample, an additional ^{1}H feature at 8.5 ppm is emerged which could be attributed to the formation of NH-water labile species, which in agreement with the crystal structures. These labile protons species exchange with deuterium, resulting in ^{2}H-NMR peaks at the identical chemical shifts in the 8.5-6.5 ppm range. The ^{1}H peaks ~8.5 ppm are due to strong hydrogen bonding interactions between cryptand(NH)-water complexes, whereas the peaks at 6.5 ppm are due to the weak hydrogen bonding interactions between them. Upon prolonged exposure to moisture to over 6h, an increase in the ^{2}H peak (6.5 ppm) intensity is observed, indicating the weak interactions between NH-sites and water molecules. A continuous exposure of the same material to moisture for a day or more leads to the displacement of ^{2}H peaks towards 6 ppm, owing to formation of channel-like water molecules entrapped in the cryptand molecules. Similar changes are likely to occur in the ^{1}H-NMR spectra shown in the left as evidence in the different distribution of peaks in the 4-9 ppm range, however, severe overlapping of ^{1}H peak inhibits the observation of these structural changes. Overall, ^{2}H-MAS NMR is a powerful approach to study the absorption of water molecules into the cryptand ligands incorporated into the bismuth octahedra.

DFT studies

To shed light into the electronic structure of the new material we performed

DFT calculations. Figure 6a shows the electronic band structure for $(DHS)_2Pb_5Br_{14}$, including spin-orbit coupling interactions. The compound is a direct band gap semiconductor, near the high-symmetry U point of the Brillouin zone (BZ) with a value of 1.53 eV. The computed band gap is lower than the experimentally determined one at 2 eV, which is expected from the chosen level of theory (see Supporting Information). The calculated charge-carrier effective masses around the valence band maximum (VBM) and the conduction band minimum (CBM) near the U point are found to be approximately 0.16 m_0 and 0.25 m_0 for electrons and holes, respectively. Similar moderate band dispersion has been recorded before for 0D Bi(III) iodide compounds.[82]

The density of states plot in Figure S7 shows that the valence and conduction band regions near the VBM and CBM edges are dominated by the bismuth and iodide species in $(DHS)Bi_2I_8$, similar to other metal halide semiconductors. Specifically, at the region near the VBM, the states are dominated by the 5*p* orbitals of the I atoms, whereas near the CBM, the region is predominantly composed of the 6*p* orbitals of Bi atoms and partially of the 5*p* of the I atoms. The states of the species composing the organic linkers are found deep in the valance and conduction band regions and, therefore, are not expected to contribute to the electrical and optical properties of the material.

Towards evaluating the effect of H_2O inclusion in the structure we calculated and analyzed the thermodynamic stability of the material, by including H_2O molecules in the DHS linkers. The geometry of the structure was optimized, with one, two, and four linkers, each containing one H_2O molecule. The results show that the water-containing systems are more stable than the pristine counterpart (without H_2O) by -0.51 eV (-49.21 kJ/mol), -1.20 eV (-115.8 kJ/mol), -2.03 eV (-195.87 kJ/mol), and -2.41 eV (-232.53 kJ/mol) per formula unit, for the systems with one, two, three, and four H_2O molecules, respectively (one H_2O per linker). Insignificant changes in the lattice parameters were observed by the inclusion of H_2O; in-plane lattice parameters *a* and *b* slightly decreased after including H_2O for the system with four H_2O molecules compared to those of the pristine structure. Inversely, the out-of-plane parameter *c* enlarged with the H_2O content, with the largest value of 0.3% for the system with four H_2O molecules (Table S5). The spatial arrangement of the H_2O molecule inside the linker adopts a particular configuration. Figure S8 shows the final arrangement of the H_2O molecule after structural relaxation. The molecule is located relatively in the center of the entrance of the rounded pocket-like linker. Moderate hydrogen bond interactions are observed between the hydrogen atoms of the H_2O molecules and the closest oxygen

atoms of the linkers, laying at an average bond distance of 2.05 Å.

Moreover, electronic structure analysis shows that the inclusion of H_2O inside the linkers does not affect the electronic properties of the material. Figures 6b c, d display the band structures of the materials with H_2O inside the linkers compared to the those of the pristine analogue, Figure 6a. The band gap remains the same and the incorporation of H_2O does not alter the dispersion and the degeneracy of the bands. The only exception is found when the four linkers of the system contain each one H_2O molecule. In that case, the band dispersion slightly changed by shifting apart the lowest degenerate conduction band from the second lowest band and the highest valence band from the second highest band, which induced a miniscule decrease in the band gap.

Furthermore, DFT studies assisted in supporting the experimental studies in regard to the maximum H_2O uptake of the porous structure. The number of H_2O molecules per linker was increased from one to two and four between the linkers as an additional constraint occupying the space between the linkers, which amount for twelve molecules in total. The initial and final structures before and after relaxation are displayed in Figure S9. Evidently, the final structure after geometry optimization and structural relaxation shows that one of the H_2O molecules inside each DHS linker is expelled from it and is located in the interstitial space between adjacent linkers. This means that DHS counter-cations can accommodate only one H_2O molecule, which is in excellent agreement with the experimental sorption data (see above).

Optical absorption and photoluminescence

UV-VIS diffuse reflectance studies of (DHS)Bi_2I_8 reveal a sharp absorption edge at 2.05 eV (Figure 7a). Upon excitation of the as made crystals at 470 nm the material exhibits broad, band-edge light emission centered at 600 nm (2.06 eV) with a full width at half maximum (FWHM) of 99 nm (0.33 eV). Corresponding emission is accompanied by an average PL decay lifetime of 3 ns (Figure S10), determined by time-correlated single-photon counting (TCSPC) spectroscopy measurements. Multi-exponential fitting of the emission decay curve reveals two exponential components with time constants of 0.7 and 4.4 ns. This emission performance is consistent with other 0D Bi(III) iodides, such as $MA_3Bi_2I_9$, which exhibits band-edge excitonic radiative luminescence.[98] Photoluminescence excitation (PLE) studies revealed a uniform emission peak profile centered at 600 nm upon exciting the sample from 410 nm to 485 nm (Figure 7b). It is pointed out that water treatment had a minuscule impact

on the optical properties. Corresponding absorbance spectra of the fresh and 9-month water treated samples are exactly the same (Figure 7d), while the emission spectrum of the 6-month water treated sample is almost identical to the one recorded for the fresh sample (Figure 7c). There is no shift in the PL peak position, rather a small increase in the FWHM from 99 nm to 102 nm for the fresh and water treated one respectively.

Antibacterial studies

Optical density (OD) measurement at a wavelength of 600 nm is used to evaluate the material's inhibition activity against both Gram-negative and Gram-positive bacteria (Figure 8a). After exposure of bacterial samples to 1 mg mL^{-1} and 10 mg mL^{-1} material for 16 h, the growth of Gram-positive bacterial strains was prevented significantly by showing much lower OD_{600} value in comparison with the negative control. At as low as 1 mg mL^{-1}, material can completely suppress the growth of six strains of bacteria (*K. pneumonia*, *P. aeruginosa, E. coli,* MRSA, MRSE and VREF), including multi-drug resistant strains. The inhibition can be directly visualized as the wells with untreated cells were turbid, but after incubation with material, the bacterial solution becomes completely clear (Figure 8b). This result also demonstrates the killing activity in MRSA, MRSE and VREF strains. Notably, PXRD studies of the recovered material, after the antibacterial essay, reveal that the structural integrity is maintained as the experimental patterns are identical to the calculated one (Figure S11). The antibacterial activity is further proved by standard plate counting assay (Figure 8c), in which MRSA strain is incubated with material for 16 h, diluted and grown in agar plate for another 12 h or 24 h, respectively. In contrast with countless colonies in the negative control, the number of bacterial colonies almost completely disappeared after material treatment.

To explore whether the material acted through a membrane-interrupting mechanism, fluorescence microscopy imaging was conducted. Among the fluorescent probes, 4,6-diamidino-2-phenylindole (DAPI) can pass through the intact cell membrane and bind strongly with adenine–thymine-rich regions in DNA. Another notable stain, propidium iodide (PI) can also bind with DNA but is not membrane permeable. Both are commonly used to evaluate cell viability. Therefore, after no treatment and material treatment, MRSA is stained by both DAPI and PI and imaged under a confocal microscope. As shown in Figure 9a, in negative control with live cells, only DAPI could enter cells and the blue fluorescence signal could be observed.

However, in treated cells, the red signal from PI is observed in addition to the blue signal, indicating that the cell membrane is damaged by material and thus cellular contents like DNA are exposed to bind with PI. The direct visualization of the disrupted membrane of MRSA is realized by TEM imaging (Figure 9b). Compared with the MRSA cells which have an intact membrane in the negative control, the cells incubated with material have lost their membrane integrity.

CONCLUSIONS

A new member of the PMHS family of materials is presented, namely (DHS)Bi_2I_8. The corresponding compound is an ultra-micorporous, visible light semiconductor with superior water stability among metal halide materials. Gas and vapor sorption studies revealed that (DHS)Bi_2I_8 can reversibly adsorb H_2O and D_2O but is impervious to N_2 and CO_2. Apparently, the presence of the organic part of the structure is essential not only for generating porosity but also for rendering (DHS)Bi_2I_8 water stable for more than a year. ssNMR studies verified the incorporation of H_2O and D_2O in the DHS cavities, while DFT calculations elucidated that H_2O inclusion does not affect the electronic properties. In addition to porosity, the material exhibits band-edge emission at RT, a property that is maintained after 6 months in water. Generating porosity to hybrid semiconductors is expected to render them proper for unexplored applications beyond photovoltaics, such as solid-state batteries and sensing.

Moreover, Bi(III) metal halide materials have been tested recently as antibacterial agents. In this regard, we evaluated the antibacterial performance of (DHS)Bi_2I_8 against both Gram-positive and negative bacteria. Interestingly, OD_{600nm} and plate counting assays demonstrate that it can completely suppress the growth of six strains of bacteria (*K. pneumonia*, *P. aeruginosa, E. coli,* MRSA, MRSE and VREF), including multi-drug resistant strains. TEM and fluorescence studies shed light on the underlying mechanism, revealing that the treated cell membranes rapture upon contact with the material, as it is recorded for other semiconductor antibacterial agents. Notably, the fact that (DHS)Bi_2I_8 is a visible light semiconductor with record water stability and composition of non-toxic, biocompatible elements renders it proper for applications beyond energy storage and generation to water purification, disinfection and antibacterial coatings on everyday touched surfaces and personal protective equipment.

ASSOCIATED CONTENT

Supporting Information

This material is available free of charge at http://pubs.acs.org.

Supplementary figures and tables about material characterization, X-ray diffraction measurements, photoluminescence measurements, thermogravimetric analysis, ssNMR, EDS, and SEM studies.

Accession Codes

CCDC 2247024 contains the supplementary crystallographic data for this paper. This data can be obtained free of charge via www.ccdc.cam.ac.uk/data_request/cif,orbyemailingdata_request@ccdc.cam.ac.uk, or by contacting The Cambridge Crystallographic Data Centre, 12 Union Road, Cambridge CB2 1EZ, UK; fax: +44 1223 336033.

AUTHOR INFORMATION

Corresponding Author

spanopoulos@usf.edu

[#]These authors contributed equally.

Notes

The authors declare no competing financial interest.

ACKNOWLEDGMENT

This work was primarily supported by USF startup funds. Use of the Advanced Photon Source at Argonne National Laboratory was supported by the U. S. Department of Energy, Office of Science, Office of Basic Energy Sciences, under Contract No. DE-AC02-06CH11357. JC acknowledges support from NIH 5R01AI152416 and 5R01AI149852.

REFERENCES

1. Koji, Y.; Hiroshi, K.; Takashi, M.; Tsutomu, O.; Sumio, I., Structural Phase Transition and Electrical Conductivity of the Perovskite $CH_3NH_3Sn_{1-x}Pb_xBr_3$ and $CsSnBr_3$, *Bull. Chem. Soc. Jpn.* **1990,** *63*, 2521-2525.
2. Stoumpos, C. C.; Malliakas, C. D.; Kanatzidis, M. G., Semiconducting Tin and Lead Iodide Perovskites with Organic Cations: Phase Transitions, High Mobilities, and Near-Infrared Photoluminescent Properties, *Inorg. Chem.* **2013,** *52*, 9019-9038.
3. Jeon, N. J.; Noh, J. H.; Yang, W. S.; Kim, Y. C.; Ryu, S.; Seo, J.; Seok, S. I., Compositional Engineering of Perovskite Materials for High-performance Solar Cells, *Nature* **2015,** *517*, 476.
4. Tsai, H.; Nie, W.; Blancon, J.-C.; Stoumpos, C. C.; Asadpour, R.; Harutyunyan, B.; Neukirch, A. J.; Verduzco, R.; Crochet, J. J.; Tretiak, S.; Pedesseau, L.; Even, J.; Alam, M. A.; Gupta, G.; Lou, J.; Ajayan, P. M.; Bedzyk, M. J.; Kanatzidis, M. G.; Mohite, A. D., High-efficiency Two-dimensional Ruddlesden–Popper Perovskite Solar Cells, *Nature* **2016,** *536*, 312.
5. Zhang, L.; Yang, X.; Jiang, Q.; Wang, P.; Yin, Z.; Zhang, X.; Tan, H.; Yang, Y.; Wei, M.; Sutherland, B. R.; Sargent, E. H.; You, J., Ultra-bright and Highly Efficient Inorganic Based Perovskite Light-emitting Diodes, *Nat. Commun.* **2017,** *8*, 15640.
6. Luo, C.; Li, W.; Fu, J.; Yang, W., Constructing Gradient Energy Levels to Promote Exciton Energy Transfer for Photoluminescence Controllability of All-Inorganic Perovskites and Application in Single-Component WLEDs, *Chem. Mater.* **2019,** *31*, 5616-5624.
7. He, Y.; Ke, W.; Alexander, G. C. B.; McCall, K. M.; Chica, D. G.; Liu, Z.; Hadar, I.; Stoumpos, C. C.; Wessels, B. W.; Kanatzidis, M. G., Resolving the Energy of γ-Ray Photons with $MAPbI_3$ Single Crystals, *ACS Photonics* **2018,** *5*, 4132-4138.
8. Yakunin, S.; Benin, B. M.; Shynkarenko, Y.; Nazarenko, O.; Bodnarchuk, M. I.; Dirin, D. N.; Hofer, C.; Cattaneo, S.; Kovalenko, M. V., High-resolution Remote Thermometry and Thermography Using Luminescent Low-dimensional Tin-halide Perovskites, *Nature Mater.* **2019,** *18*, 846-852.
9. Hong, Z.; Chong, W. K.; Ng, A. Y. R.; Li, M.; Ganguly, R.; Sum, T. C.; Soo, H. S., Hydrophobic Metal Halide Perovskites for Visible-Light Photoredox C−C Bond Cleavage and Dehydrogenation Catalysis, *Angew. Chem. Int. Ed.* **2019,** *58*, 3456-3460.
10. Zhu, H.; Fu, Y.; Meng, F.; Wu, X.; Gong, Z.; Ding, Q.; Gustafsson, M. V.; Trinh, M. T.; Jin, S.; Zhu, X. Y., Lead Halide Perovskite Nanowire Lasers with Low Lasing Thresholds and High Quality Factors, *Nature Mater.* **2015,** *14*, 636.
11. Leng, K.; Abdelwahab, I.; Verzhbitskiy, I.; Telychko, M.; Chu, L.; Fu, W.; Chi, X.; Guo, N.; Chen, Z.; Chen, Z.; Zhang, C.; Xu, Q.-H.; Lu, J.; Chhowalla, M.; Eda, G.; Loh, K. P., Molecularly Thin two-dimensional Hybrid Perovskites with Tunable Optoelectronic Properties due to Reversible Surface Relaxation, *Nature Mater.* **2018,** *17*, 908-914.
12. Manser, J. S.; Christians, J. A.; Kamat, P. V., Intriguing Optoelectronic Properties of Metal Halide Perovskites, *Chem. Rev.* **2016,** *116*, 12956-13008.
13. Chouhan, L.; Ghimire, S.; Subrahmanyam, C.; Miyasaka, T.; Biju, V., Synthesis, Optoelectronic Properties and Applications of Halide Perovskites, *Chem. Soc. Rev.* **2020,** *49*, 2869-2885.
14. Tu, Q.; Spanopoulos, I.; Hao, S.; Wolverton, C.; Kanatzidis, M. G.; Shekhawat, G. S.; Dravid, V. P., Out-of-Plane Mechanical Properties of 2D Hybrid Organic–Inorganic Perovskites by Nanoindentation, *ACS Appl. Mater. Interfaces* **2018,** *10*, 22167-22173.
15. Tu, Q.; Spanopoulos, I.; Yasaei, P.; Stoumpos, C. C.; Kanatzidis, M. G.; Shekhawat, G. S.; Dravid, V. P., Stretching and Breaking of Ultrathin 2D Hybrid Organic–Inorganic Perovskites, *ACS Nano* **2018,** *12*, 10347-10354.
16. Ono, L. K.; Qi, Y.; Liu, S., Progress toward Stable Lead Halide Perovskite Solar Cells, *Joule* **2018,** *2*, 1961-1990.
17. Meng, D.; Xue, J.; Zhao, Y.; Zhang, E.; Zheng, R.; Yang, Y., Configurable Organic Charge Carriers toward Stable Perovskite Photovoltaics, *Chem. Rev.* **2022,** *122*, 14954-14986.
18. Jana, A.; Kim, K. S., Water-Stable, Fluorescent Organic−Inorganic Hybrid and Fully Inorganic Perovskites, *ACS Energy Lett.* **2018,** *3*, 2120-2126.
19. Wang, H.; Zhang, Z.; Milić, J. V.; Tan, L.; Wang, Z.; Chen, R.; Jing, X.; Yi, C.; Ding, Y.; Li, Y.; Zhao, Y.; Zhang, X.; Hagfeldt, A.; Grätzel, M.; Luo, J., Water Stable Haloplumbate Modulation for Efficient and Stable Hybrid Perovskite Photovoltaics, *Adv. Energy Mater.* **2021,** *11*, 2101082.
20. Azmy, A.; Li, S.; Angeli, G. K.; Welton, C.; Raval, P.; Li, M.; Zibouche, N.; Wojtas, L.; Reddy, G. N. M.; Guo, P.; Trikalitis, P. N.; Spanopoulos, I., Porous and Water Stable 2D Hybrid Metal Halide with Broad

Light Emission and Selective H_2O Vapor Sorption, *Angew. Chem. Int. Ed.* **2023,** *62*, e202218429.
21. Park, N.-G.; Grätzel, M.; Miyasaka, T.; Zhu, K.; Emery, K., Towards Stable and Commercially Available Perovskite Solar Cells, *Nat. Energy* **2016,** *1*, 16152.
22. Zheng, Y.; Wei, M.; Wu, H.; Li, F.; Ling, D., Antibacterial Metal Nanoclusters, *J. Nanobiotechnology* **2022,** *20*, 328.
23. Shetu, S. A.; Sanchez-Palestino, L. M.; Rivera, G.; Bandyopadhyay, D., Medicinal Bismuth: Bismuth-organic Frameworks as Pharmaceutically Privileged Compounds, *Tetrahedron* **2022,** *129*, 133117.
24. Ong, Y. C.; Roy, S.; Andrews, P. C.; Gasser, G., Metal Compounds against Neglected Tropical Diseases, *Chem. Rev.* **2019,** *119*, 730-796.
25. Irfan, M.; Almotiri, A.; AlZeyadi, Z. A., Antimicrobial Resistance and Its Drivers-A Review, *Antibiotics* **2022,** *11*, 1362.
26. Antimicrobial Resistance, accessed on 03/25/2023, *World Health Organization* **2021**, https://www.who.int/news-room/fact-sheets/detail/antimicrobial-resistance.
27. Chakraborty, N.; Jha, D.; Roy, I.; Kumar, P.; Gaurav, S. S.; Marimuthu, K.; Ng, O.-T.; Lakshminarayanan, R.; Verma, N. K.; Gautam, H. K., Nanobiotics Against Antimicrobial Resistance: Harnessing the Power of Nanoscale Materials and Technologies, *J. Nanobiotechnology* **2022,** *20*, 375.
28. da Cunha, N. B.; Cobacho, N. B.; Viana, J. F. C.; Lima, L. A.; Sampaio, K. B. O.; Dohms, S. S. M.; Ferreira, A. C. R.; de la Fuente-Núñez, C.; Costa, F. F.; Franco, O. L.; Dias, S. C., The Next Generation of Antimicrobial Peptides (AMPs) as Molecular Therapeutic Tools for the Treatment of Diseases with Social and Economic Impacts, *Drug Discov. Today* **2017,** *22*, 234-248.
29. Li, L.; Cao, L.; Xiang, X.; Wu, X.; Ma, L.; Chen, F.; Cao, S.; Cheng, C.; Deng, D.; Qiu, L., ROS-Catalytic Transition-Metal-Based Enzymatic Nanoagents for Tumor and Bacterial Eradication, *Adv. Funct. Mater.* **2022,** *32*, 2107530.
30. McCalla, D. R.; Reuvers, A.; Kaiser, C., Mode of Action of Nitrofurazone, *J. Bacteriol.* **1970,** *104*, 1126-1134.
31. Rafailidis, P. I.; Ioannidou, E. N.; Falagas, M. E., Ampicillin/Sulbactam, *Drugs* **2007,** *67*, 1829-1849.
32. Huttner, A.; Verhaegh, E. M.; Harbarth, S.; Muller, A. E.; Theuretzbacher, U.; Mouton, J. W., Nitrofurantoin Revisited: a Systematic Review and Meta-analysis of Controlled Trials, *J. Antimicrob. Chemother.* **2015,** *70*, 2456-2464.
33. Wieland, M.; Holm, M.; Rundlet, E. J.; Morici, M.; Koller, T. O.; Maviza, T. P.; Pogorevc, D.; Osterman, I. A.; Müller, R.; Blanchard, S. C.; Wilson, D. N., The Cyclic Octapeptide Antibiotic Argyrin B inhibits Translation by Trapping EF-G on the Ribosome During Translocation, *Proc. Natl. Acad. Sci.* **2022,** *119*, e2114214119.
34. Garner, J. P.; Heppell, P. S. J., The use of Flammacerium in British Burns Units, *Burns* **2005,** *31*, 379-382.
35. Barillo, D. J.; Barillo, A. R.; Korn, S.; Lam, K.; Attar, P. S., The Antimicrobial Spectrum of Xeroform®, *Burns* **2017,** *43*, 1189-1194.
36. Melander, R. J.; Melander, C., The Challenge of Overcoming Antibiotic Resistance: An Adjuvant Approach?, *ACS Infect. Dis.* **2017,** *3*, 559-563.
37. Lemire, J. A.; Harrison, J. J.; Turner, R. J., Antimicrobial Activity of Metals: Mechanisms, Molecular Targets and Applications, *Nat. Rev. Microbiol* **2013,** *11*, 371-384.
38. Frei, A.; Zuegg, J.; Elliott, A. G.; Baker, M.; Braese, S.; Brown, C.; Chen, F.; G. Dowson, C.; Dujardin, G.; Jung, N.; King, A. P.; Mansour, A. M.; Massi, M.; Moat, J.; Mohamed, H. A.; Renfrew, A. K.; Rutledge, P. J.; Sadler, P. J.; Todd, M. H.; Willans, C. E.; Wilson, J. J.; Cooper, M. A.; Blaskovich, M. A. T., Metal Complexes as a Promising Source for New Antibiotics, *Chem. Sci.* **2020,** *11*, 2627-2639.
39. Anthony, E. J.; Bolitho, E. M.; Bridgewater, H. E.; Carter, O. W. L.; Donnelly, J. M.; Imberti, C.; Lant, E. C.; Lermyte, F.; Needham, R. J.; Palau, M.; Sadler, P. J.; Shi, H.; Wang, F.-X.; Zhang, W.-Y.; Zhang, Z., Metallodrugs are Unique: Opportunities and Challenges of Discovery and Development, *Chem. Sci.* **2020,** *11*, 12888-12917.
40. Wang, F.; Habtemariam, A.; van der Geer, E. P. L.; Fernández, R.; Melchart, M.; Deeth, R. J.; Aird, R.; Guichard, S.; Fabbiani, F. P. A.; Lozano-Casal, P.; Oswald, I. D. H.; Jodrell, D. I.; Parsons, S.; Sadler, P. J., Controlling Ligand Substitution Reactions of Organometallic Complexes: Tuning Cancer Cell Cytotoxicity, *Proc. Natl. Acad. Sci.* **2005,** *102*, 18269-18274.
41. Warnes, S. L.; Caves, V.; Keevil, C. W., Mechanism of Copper Surface Toxicity in Escherichia coli O157:H7 and Salmonella involves Immediate Membrane Depolarization Followed by Slower Rate of

DNA Destruction which Differs from that Observed for Gram-positive Bacteria, *Environ. Microbiol.* **2012,** *14*, 1730-1743.
42. Zhang, P.; Sadler, P. J., Redox-Active Metal Complexes for Anticancer Therapy, *Eur. J. Inorg. Chem.* **2017,** *2017*, 1541-1548.
43. Frei, A.; Verderosa, A. D.; Elliott, A. G.; Zuegg, J.; Blaskovich, M. A. T., Metals to Combat Antimicrobial Resistance, *Nat. Rev. Chem.* **2023,** *7*, 202-224.
44. Gasser, G.; Metzler-Nolte, N., The Potential of Organometallic Complexes in Medicinal Chemistry, *Curr. Opin. Chem. Biol.* **2012,** *16*, 84-91.
45. Gianferrara, T.; Bratsos, I.; Alessio, E., A Categorization of Metal Anticancer Compounds Based on their Mode of Action, *Dalton Trans.* **2009**, 7588-7598.
46. Wang, X.; Xu, A.; Liu, Y., Combined Biological Effects of Silver Nanoparticles and Heavy Metals in Different Target Cell Lines, *Environ Sci Pollut Res.* **2022,** *29*, 16324-16331.
47. Novak, M. S.; Büchel, G. E.; Keppler, B. K.; Jakupec, M. A., Biological Properties of Novel Ruthenium- and Osmium-nitrosyl Complexes with Azole Heterocycles, *J. Biol. Inorg. Chem.* **2016,** *21*, 347-356.
48. Mehra, L.; Mehra, S.; Tiwari, N.; Singh, T.; Rawat, H.; Belagavi, S.; Jaimini, A.; Mittal, G., Fabrication, Characterization and Evaluation of the Efficacy of Gelatin/hyaluronic Acid Microporous Scaffolds Suffused with Aloe-vera in a Rat Burn Model, *J. Biomater. Appl.* **2022,** *36*, 1346-1358.
49. Kanatzidis, M.; Sun, H.; Dehnen, S., Bismuth—The Magic Element, *Inorg. Chem.* **2020,** *59*, 3341-3343.
50. Khan, M. H.; Cai, M.; Li, S.; Zhang, Z.; Zhang, J.; Wen, X.; Sun, H.; Liang, H.; Yang, F., Developing a Binuclear Multi-target Bi(III) Complex by Optimizing 2-acetyl-3-ethylpyrazine Thiosemicarbazides, *Eur. J. Med. Chem.* **2019,** *182*, 111616.
51. Duffin, R. N.; Werrett, M. V.; Andrews, P. C., Chapter Seven - Antimony and Bismuth as Antimicrobial Agents. In *Advances in Inorganic Chemistry*, Sadler, P. J.; van Eldik, R., Eds. Academic Press: 2020; Vol. 75, pp 207-255.
52. Griffith, D. M.; Li, H.; Werrett, M. V.; Andrews, P. C.; Sun, H., Medicinal Chemistry and Biomedical Applications of Bismuth-based Compounds and Nanoparticles, *Chem. Soc. Rev.* **2021,** *50*, 12037-12069.
53. Kumar, S.; Schmitt, C.; Gorgette, O.; Marbouty, M.; Duchateau, M.; Gianetto, Q. G.; Matondo, M.; Guigner, J.-M.; Reuse, H. D., Bacterial Membrane Vesicles as a Novel Strategy for Extrusion of Antimicrobial Bismuth Drug in Helicobacter pylori, *mBio* **2022,** *13*, e01633-01622.
54. Ouerghi, Z.; Gornitzka, H.; Temel, E.; Dridi, I.; Kefi, R., A new non-centrosymmetric Chlorobismuthate(III) Hybrid Material: Crystal structure, Optical Properties and Antibacterial Study, *J. Mol. Struct.* **2019,** *1181*, 338-347.
55. Ben Ali, S.; Feki, A.; Ferretti, V.; Nasri, M.; Belhouchet, M., Crystal Structure, Spectroscopic Measurement, Optical Properties, Thermal Studies and Biological Activities of a New Hybrid Material Containing Iodide Anions of Bismuth(iii), *RSC Adv.* **2020,** *10*, 35174-35184.
56. Aygun, O.; Grześkiewicz, A. M.; Banti, C. N.; Hadjikakou, S. K.; Kubicki, M.; Ozturk, I. I., Monomeric Octahedral Bismuth(III) Benzaldehyde-N1-alkyl thiosemicarbazones: Synthesis, Characterization and Biological Properties, *Polyhedron* **2022,** *215*, 115683.
57. Ozturk, I. I.; Banti, C. N.; Hadjikakou, S. K.; Panagiotou, N.; Tasiopoulos, A. J., Bismuth(III) Halide Complexes of Aromatic Thiosemicarbazones: Synthesis, Structural Characterization and Biological Evaluation, *Polyhedron* **2021,** *208*, 115388.
58. Turk, K.; Grześkiewicz, A. M.; Banti, C. N.; Hadjikakou, S. K.; Kubicki, M.; Ozturk, I. I., Synthesis, Characterization, and Biological Properties of mono-, di- and Poly-nuclear Bismuth(III) Halide Complexes Containing Thiophene-2-carbaldehyde Thiosemicarbazones, *J. Inorg. Biochem.* **2022,** *237*, 111987.
59. Scaccaglia, M.; Rega, M.; Bacci, C.; Giovanardi, D.; Pinelli, S.; Pelosi, G.; Bisceglie, F., Bismuth Complex of Quinoline Thiosemicarbazone Restores Carbapenem Sensitivity in NDM-1-positive Klebsiella Pneumoniae, *J. Inorg. Biochem.* **2022,** *234*, 111887.
60. Maliha, M.; Tan, B.; Wong, K.; Miri, S.; Brammananth, R.; Coppel, R. L.; Werrett, M.; Andrews, P. C.; Batchelor, W., Bismuth Phosphinato Incorporated Antibacterial Filter Paper for Drinking Water Disinfection, *Colloids Surf, A Physicochem. Eng. Asp.* **2021,** *627*, 127167.
61. Karim, N.; Afroj, S.; Lloyd, K.; Oaten, L. C.; Andreeva, D. V.; Carr, C.; Farmery, A. D.; Kim, I.-D.; Novoselov, K. S., Sustainable Personal Protective Clothing for Healthcare Applications: A Review, *ACS Nano* **2020,** *14*, 12313-12340.
62. Zheng, C. R.; Li, S.; Ye, C.; Li, X.; Zhang, C.; Yu, X., Particulate Respirators Functionalized with

Silver Nanoparticles Showed Excellent Real-Time Antimicrobial Effects against Pathogens, *Environ. Sci. Technol.* **2016,** *50*, 7144-7151.
63. Maliha, M.; Herdman, M.; Brammananth, R.; McDonald, M.; Coppel, R.; Werrett, M.; Andrews, P.; Batchelor, W., Bismuth Phosphinate Incorporated Nanocellulose Sheets with Antimicrobial and Barrier Properties for Packaging Applications, *J. Clean. Prod.* **2020,** *246*, 119016.
64. Bruker, APEX4. Bruker AXS LLC, Madison, Wisconsin, USA., **2022**.
65. Bruker, SAINT. Bruker AXS LLC, Madison, Wisconsin, USA., **2022**.
66. Krause, L.; Herbst-Irmer, R.; Sheldrick, G. M.; Stalke, D., Comparison of Silver and Molybdenum Microfocus X-ray Sources for Single-crystal Structure Determination, *J Appl Crystallogr* **2015,** *48*, 3-10.
67. Sheldrick, G., SHELXT - Integrated Space-group and Crystal-structure Determination, *Acta Crystallogr. Sect. A* **2015,** *71*, 3-8.
68. Sheldrick, G., Crystal Structure Refinement with SHELXL, *Acta Crystallogr. Sect. C* **2015,** *71*, 3-8.
69. Dolomanov, O. V.; Bourhis, L. J.; Gildea, R. J.; Howard, J. A. K.; Puschmann, H., OLEX2: a Complete Structure Solution, Refinement and Analysis Program, *J. Appl. Crystallogr.* **2009,** *42*, 339-341.
70. Spek, A., Single-crystal Structure Validation with the Program PLATON, *J. Appl. Crystallogr.* **2003,** *36*, 7-13.
71. Toby, B., CMPR - a Powder Diffraction Toolkit, *J. Appl. Crystallogr.* **2005,** *38*, 1040-1041.
72. Gate, L. F., Comparison of the Photon Diffusion Model and Kubelka-Munk Equation with the Exact Solution of the Radiative Transport Equation, *Appl. Opt.* **1974,** *13*, 236-238.
73. Giannozzi, P.; Andreussi, O.; Brumme, T.; Bunau, O.; Buongiorno Nardelli, M.; Calandra, M.; Car, R.; Cavazzoni, C.; Ceresoli, D.; Cococcioni, M.; Colonna, N.; Carnimeo, I.; Dal Corso, A.; de Gironcoli, S.; Delugas, P.; DiStasio, R. A.; Ferretti, A.; Floris, A.; Fratesi, G.; Fugallo, G.; Gebauer, R.; Gerstmann, U.; Giustino, F.; Gorni, T.; Jia, J.; Kawamura, M.; Ko, H. Y.; Kokalj, A.; Küçükbenli, E.; Lazzeri, M.; Marsili, M.; Marzari, N.; Mauri, F.; Nguyen, N. L.; Nguyen, H. V.; Otero-de-la-Roza, A.; Paulatto, L.; Poncé, S.; Rocca, D.; Sabatini, R.; Santra, B.; Schlipf, M.; Seitsonen, A. P.; Smogunov, A.; Timrov, I.; Thonhauser, T.; Umari, P.; Vast, N.; Wu, X.; Baroni, S., Advanced Capabilities for Materials Modelling with Quantum ESPRESSO, *J. Phys.: Condens. Matter* **2017,** *29*, 465901.
74. Giannozzi, P.; Baroni, S.; Bonini, N.; Calandra, M.; Car, R.; Cavazzoni, C.; Ceresoli, D.; Chiarotti, G. L.; Cococcioni, M.; Dabo, I.; Dal Corso, A.; de Gironcoli, S.; Fabris, S.; Fratesi, G.; Gebauer, R.; Gerstmann, U.; Gougoussis, C.; Kokalj, A.; Lazzeri, M.; Martin-Samos, L.; Marzari, N.; Mauri, F.; Mazzarello, R.; Paolini, S.; Pasquarello, A.; Paulatto, L.; Sbraccia, C.; Scandolo, S.; Sclauzero, G.; Seitsonen, A. P.; Smogunov, A.; Umari, P.; Wentzcovitch, R. M., QUANTUM ESPRESSO: a Modular and Open-source Software Project for Quantum Simulations of Materials, *J. Phys.: Condens. Matter* **2009,** *21*, 395502.
75. Perdew, J. P.; Burke, K.; Ernzerhof, M., Generalized Gradient Approximation Made Simple, *Phys. Rev. Lett.* **1996,** *77*, 3865-3868.
76. Perdew, J. P.; Ruzsinszky, A.; Csonka, G. I.; Vydrov, O. A.; Scuseria, G. E.; Constantin, L. A.; Zhou, X.; Burke, K., Restoring the Density-Gradient Expansion for Exchange in Solids and Surfaces, *Phys. Rev. Lett.* **2008,** *100*, 136406.
77. Grimme, S.; Antony, J.; Ehrlich, S.; Krieg, H., A Consistent and Accurate ab initio Parametrization of Density Functional Dispersion Correction (DFT-D) for the 94 elements H-Pu, *J. Chem. Phys.* **2010,** *132*, 154104.
78. Grimme, S.; Ehrlich, S.; Goerigk, L., Effect of the Damping Function in Dispersion Corrected Density Functional Theory, *J. Comput. Chem.* **2011,** *32*, 1456-1465.
79. Vanderbilt, D., Soft Self-consistent Pseudopotentials in a Generalized eigenvalue Formalism, *Phys. Rev. B* **1990,** *41*, 7892-7895.
80. Monkhorst, H. J.; Pack, J. D., Special Points for Brillouin-zone Integrations, *Phys. Rev. B* **1976,** *13*, 5188-5192.
81. Li, X.; Traoré, B.; Kepenekian, M.; Li, L.; Stoumpos, C. C.; Guo, P.; Even, J.; Katan, C.; Kanatzidis, M. G., Bismuth/Silver-Based Two-Dimensional Iodide Double and One-Dimensional Bi Perovskites: Interplay between Structural and Electronic Dimensions, *Chem. Mater.* **2021,** *33*, 6206-6216.
82. Lehner, A. J.; Fabini, D. H.; Evans, H. A.; Hébert, C.-A.; Smock, S. R.; Hu, J.; Wang, H.; Zwanziger, J. W.; Chabinyc, M. L.; Seshadri, R., Crystal and Electronic Structures of Complex Bismuth Iodides $A_3Bi_2I_9$ (A = K, Rb, Cs) Related to Perovskite: Aiding the Rational Design of Photovoltaics, *Chem. Mater.* **2015,** *27*, 7137-7148.
83. Spanopoulos, I.; Hadar, I.; Ke, W.; Guo, P.; Sidhik, S.; Kepenekian, M.; Even, J.; Mohite, A. D.; Schaller, R. D.; Kanatzidis, M. G., Water-Stable 1D Hybrid Tin(II) Iodide Emits Broad Light with 36% Photoluminescence Quantum Efficiency, *J. Am. Chem. Soc.* **2020,** *142*, 9028-9038.

84. Spanopoulos, I.; Hadar, I.; Ke, W.; Tu, Q.; Chen, M.; Tsai, H.; He, Y.; Shekhawat, G.; Dravid, V. P.; Wasielewski, M. R.; Mohite, A. D.; Stoumpos, C. C.; Kanatzidis, M. G., Uniaxial Expansion of the 2D Ruddlesden–Popper Perovskite Family for Improved Environmental Stability, *J. Am. Chem. Soc.* **2019,** *141*, 5518-5534.
85. Spanopoulos, I.; Ke, W.; Stoumpos, C. C.; Schueller, E. C.; Kontsevoi, O. Y.; Seshadri, R.; Kanatzidis, M. G., Unraveling the Chemical Nature of the 3D "Hollow" Hybrid Halide Perovskites, *J. Am. Chem. Soc.* **2018,** *140*, 5728-5742.
86. Kong, M.; Hu, H.; Wan, L.; Chen, M.; Gan, Y.; Wang, J.; Chen, F.; Dong, B.; Eder, D.; Wang, S., Nontoxic $(CH_3NH_3)_3Bi_2I_9$ Perovskite Solar Cells free of Hole Conductors with an Alternative Architectural Design and a Solution-processable Approach, *RSC Adv.* **2017,** *7*, 35549-35557.
87. Zhou, L.; Xu, Y.-F.; Chen, B.-X.; Kuang, D.-B.; Su, C.-Y., Synthesis and Photocatalytic Application of Stable Lead-Free $Cs_2AgBiBr_6$ Perovskite Nanocrystals, *Small* **2018,** *14*, 1703762.
88. Hoye, R. L. Z.; Brandt, R. E.; Osherov, A.; Stevanović, V.; Stranks, S. D.; Wilson, M. W. B.; Kim, H.; Akey, A. J.; Perkins, J. D.; Kurchin, R. C.; Poindexter, J. R.; Wang, E. N.; Bawendi, M. G.; Bulović, V.; Buonassisi, T., Methylammonium Bismuth Iodide as a Lead-Free, Stable Hybrid Organic–Inorganic Solar Absorber, *Chem. Eur. J.* **2016,** *22*, 2605-2610.
89. McClure, E. T.; Ball, M. R.; Windl, W.; Woodward, P. M., Cs_2AgBiX_6 (X = Br, Cl): New Visible Light Absorbing, Lead-Free Halide Perovskite Semiconductors, *Chem. Mater.* **2016,** *28*, 1348-1354.
90. Zhao, H.; Chordiya, K.; Leukkunen, P.; Popov, A.; Upadhyay Kahaly, M.; Kordas, K.; Ojala, S., Dimethylammonium Iodide Stabilized Bismuth Halide Perovskite Photocatalyst for Hydrogen Evolution, *Nano Res.* **2021,** *14*, 1116-1125.
91. Romagnoli, L.; D′Annibale, A.; Blundo, E.; Polimeni, A.; Cassetta, A.; Chita, G.; Panetta, R.; Ciccioli, A.; Latini, A., Synthesis, Structure, and Characterization of 4,4′-(Anthracene-9,10-diylbis(ethyne-2,1-diyl))bis(1-methyl-1-pyridinium) Bismuth Iodide $(C_{30}H_{22}N_2)_3Bi_4I_{18}$, an Air, Water, and Thermally Stable 0D Hybrid Perovskite with High Photoluminescence Efficiency, *Cryst. Growth Des.* **2022,** *22*, 7426-7433.
92. Ma, C.; Li, H.; Chen, M.; Liu, Y.; Zhao, K.; Liu, S., Water-Resistant Lead-Free Perovskitoid Single Crystal for Efficient X-Ray Detection, *Adv. Funct. Mater.* **2022,** *32*, 2202160.
93. Liu, G.-N.; Zhao, R.-Y.; Xu, B.; Sun, Y.; Jiang, X.-M.; Hu, X.; Li, C., Design, Synthesis, and Photocatalytic Application of Moisture-Stable Hybrid Lead-Free Perovskite, *ACS Appl. Mater. Interfaces* **2020,** *12*, 54694-54702.
94. Ockwig, N. W.; Nenoff, T. M., Membranes for Hydrogen Separation, *Chem. Rev.* **2007,** *107*, 4078-4110.
95. Furukawa, H.; Gándara, F.; Zhang, Y.-B.; Jiang, J.; Queen, W. L.; Hudson, M. R.; Yaghi, O. M., Water Adsorption in Porous Metal–Organic Frameworks and Related Materials, *J. Am. Chem. Soc.* **2014,** *136*, 4369-4381.
96. Raval, P.; Kennard, R. M.; Vasileiadou, E. S.; Dahlman, C. J.; Spanopoulos, I.; Chabinyc, M. L.; Kanatzidis, M.; Manjunatha Reddy, G. N., Understanding Instability in Formamidinium Lead Halide Perovskites: Kinetics of Transformative Reactions at Grain and Subgrain Boundaries, *ACS Energy Lett.* **2022,** *7*, 1534-1543.
97. Dahlman, C. J.; Kubicki, D. J.; Reddy, G. N. M., Interfaces in Metal Halide Perovskites Probed by solid-state NMR Spectroscopy, *J. Mater. Chem. A* **2021,** *9*, 19206-19244.
98. Zhang, L.; Liu, C.; Lin, Y.; Wang, K.; Ke, F.; Liu, C.; Mao, W. L.; Zou, B., Tuning Optical and Electronic Properties in Low-Toxicity Organic–Inorganic Hybrid $(CH_3NH_3)3Bi_2I_9$ under High Pressure, *J. Phys. Chem. Lett.* **2019,** *10*, 1676-1683.

Figures

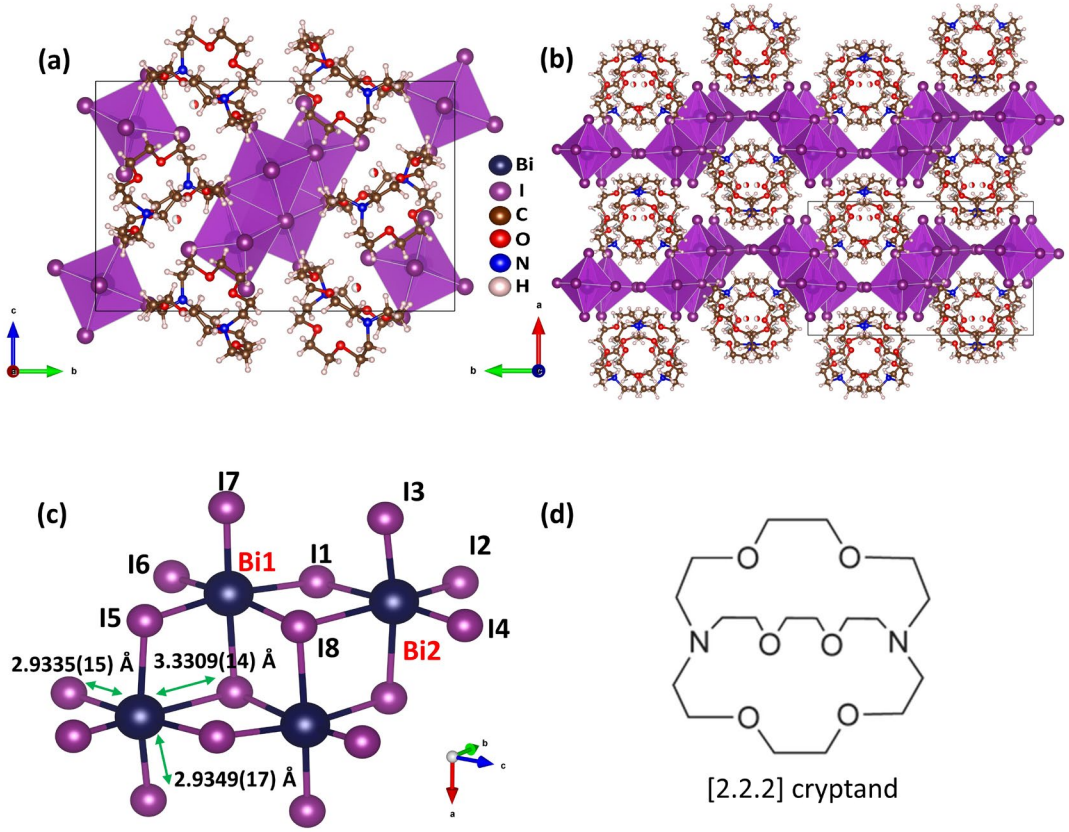

Figure 1. a) The unit cell contents of the crystal structure of (DHS)Bi_2I_8 viewing across the *α*-axis. b) Part of the crystal structure across the *c*-axis. Disordered carbon, nitrogen and oxygen atoms are omitted for clarity. c) The structure of the inorganic $[Bi_4I_{16}]^{4-}$ tetramer showing the octahedral connectivity and representative Bi-I bond lengths. d) Molecular representation of the [2.2.2] cryptand (DHS).

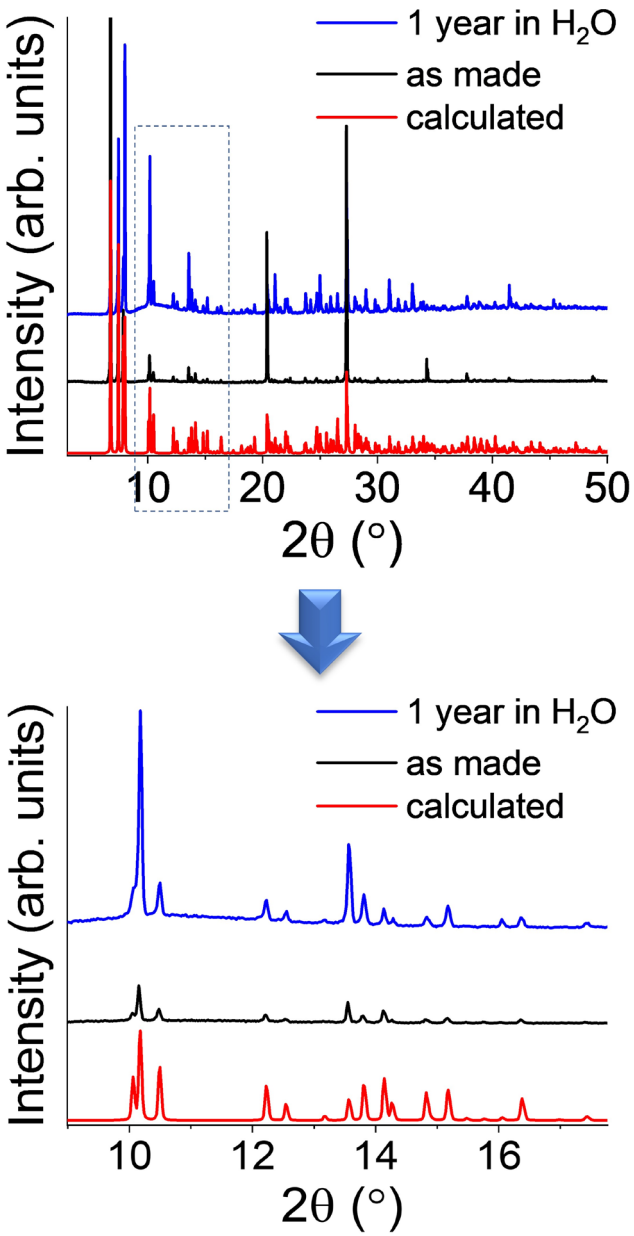

Figure 2. Top: Comparison of the PXRD patterns for the as made (DHS)Bi_2I_8 crystals and the water treated ones, to the calculated pattern based from the solved single crystal structure. Bottom: zoom into the highlighted area of the PXRD patterns from 9° to 18° 2θ verifying the high crystallinity and phase purity of the water treated sample.

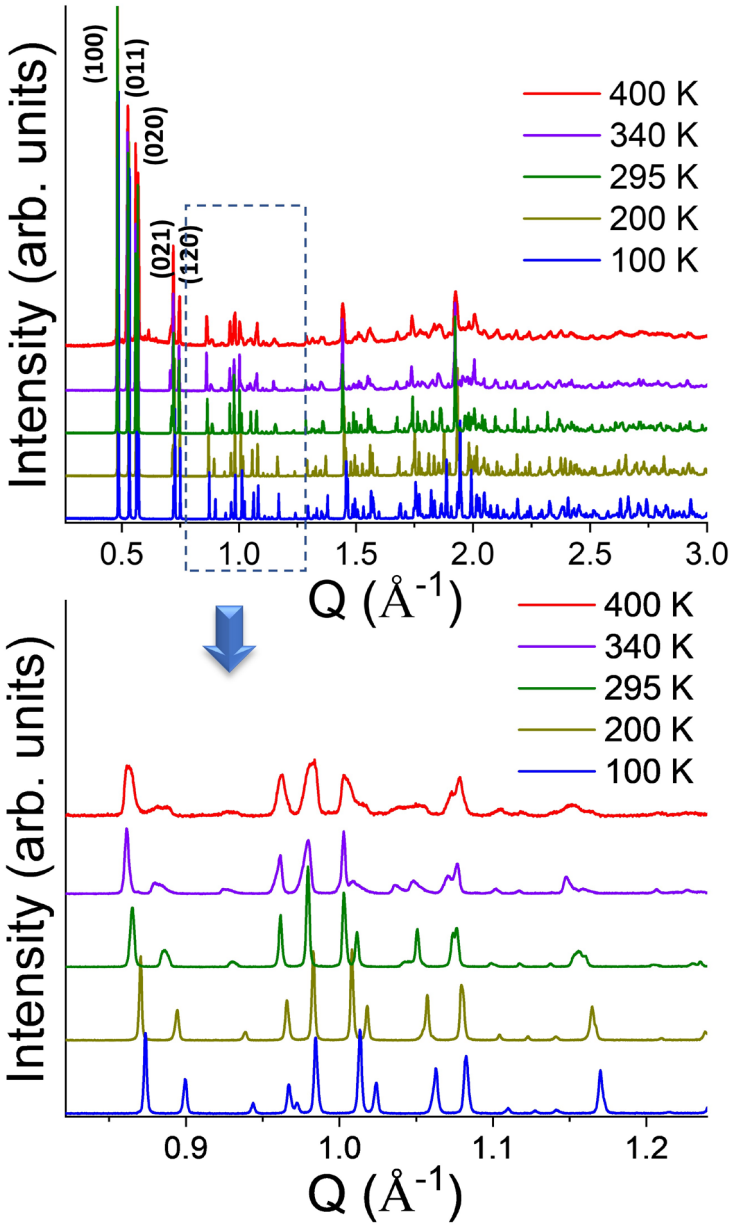

Figure 3. Top: High resolution variable temperature PXRD patterns for the (DHS)Bi_2I_8, consisting of one heating cycle. Bottom: The highlighted area is enlarged to show the shift of the diffraction peaks to lower Q values with increasing temperature, indicative of lattice thermal expansion. The material is thermally robust up to 340 K.

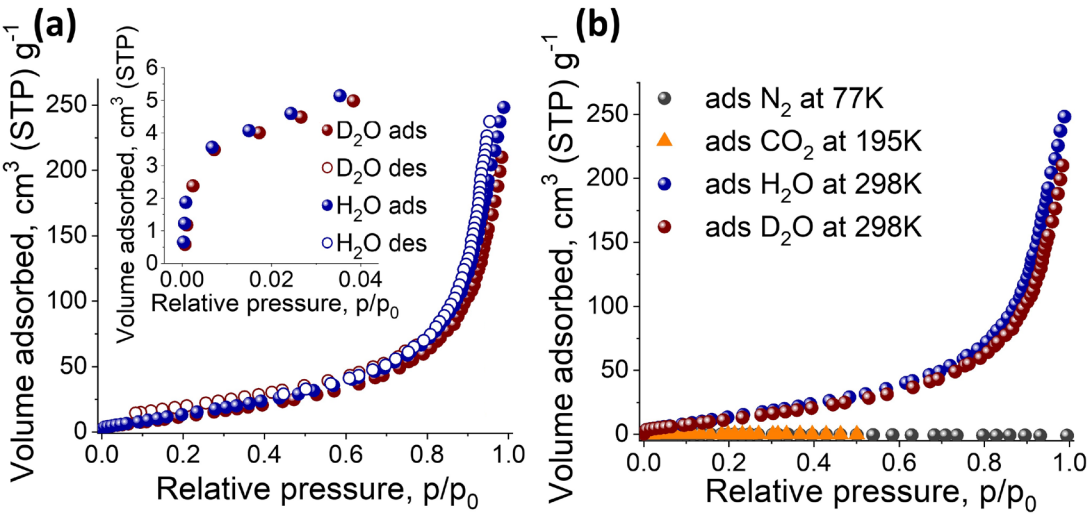

Figure 4. a) H_2O and D_2O adsorption and desorption isotherms recorded at 298K up to 1bar, the reversible character of the isotherm is indicative of physisorption of the vapor molecules in the adsorbent. The inset figure shows the sharp vapor uptake at low pressures, indicative of micropore filling. b) N_2, CO_2, H_2O and D_2O isotherms at 77 K, 195 K, and 298 K respectively. The material is impervious to N_2 and CO_2, demonstrating its ultra-microporous nature.

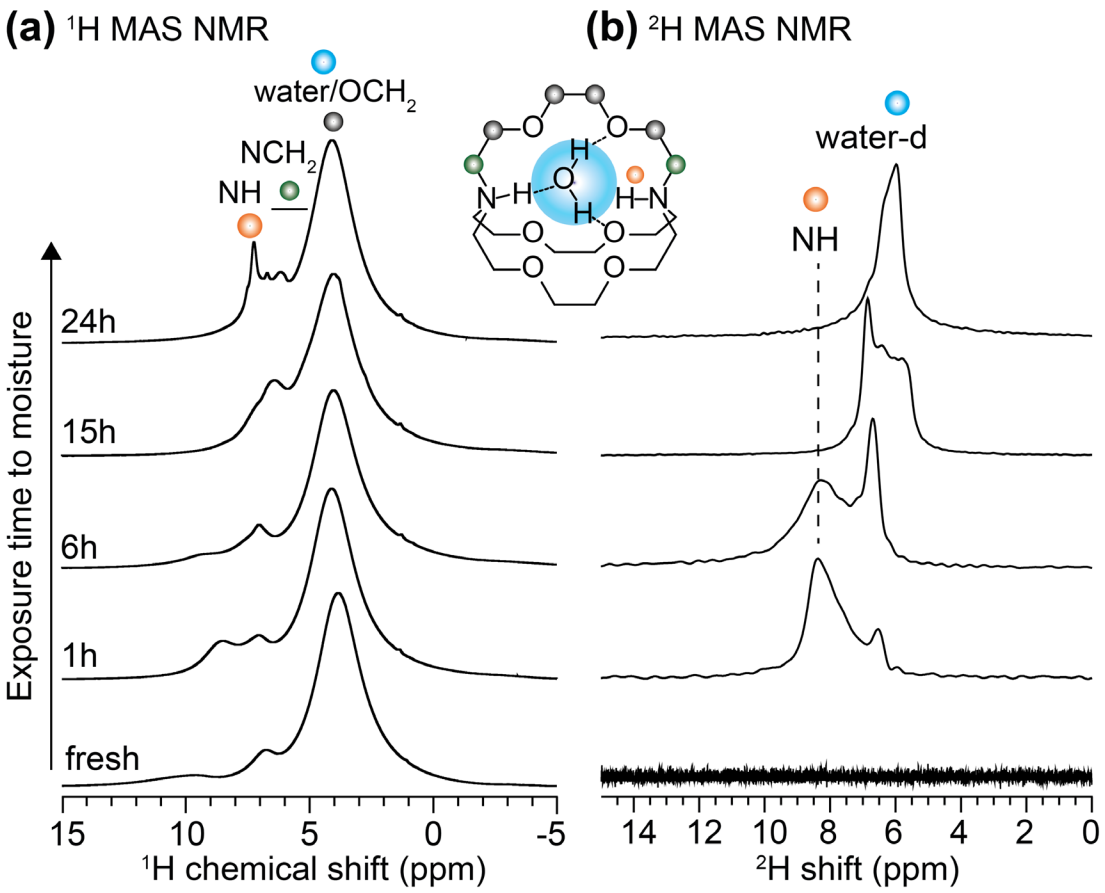

Figure 5. Solid-state (a) ^{1}H and (b) ^{2}H-MAS NMR spectra of $(DHS)Bi_2I_8$ before and after exposure to moisture at 85% relative humidity in the air. Signals correspond to -OCH_2-, -NCH_2-, H_2O/D_2O and NH/DH groups of cryptand-water complexes are resolved. The increasing uptake of water molecules by the cryptand is evident from the water-d peak in (b). All spectra were acquired at 18.8 T (Larmor frequencies of ^{1}H = 800.1 MHz and ^{2}H = 122.8 MHz) with 50 kHz magic-angle spinning.

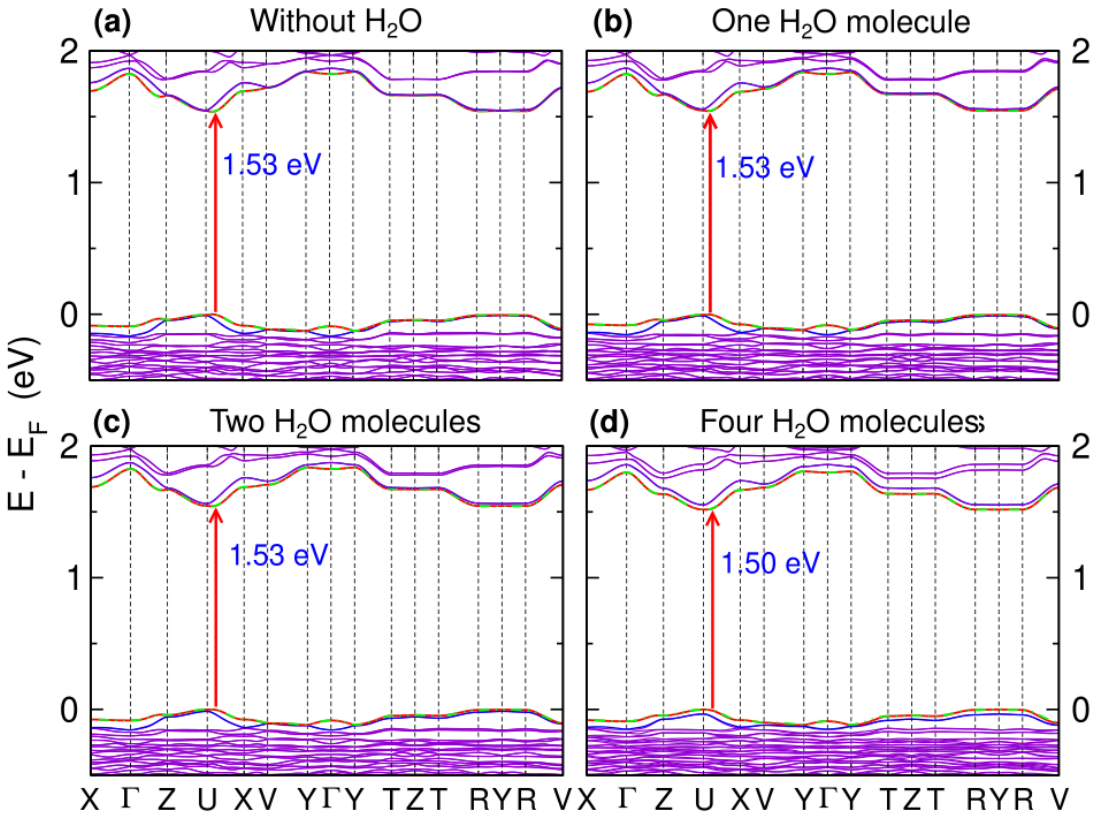

Figure 6. Band structure evolution of (DHS)Bi_2I_8 with H_2O loading, (a) pristine system, (b) with one H_2O molecule per four DHS linkers, (c) two H_2O molecules per four DHS linkers, and (d) four H_2O molecules per four DHS linkers (100% H_2O loading). Only one H_2O molecule can reside in each DHS linker. The band structures are calculated including spin-orbit coupling, green/dashed black and red/dashed black lines show the degenerate VBM and CBM, respectively.

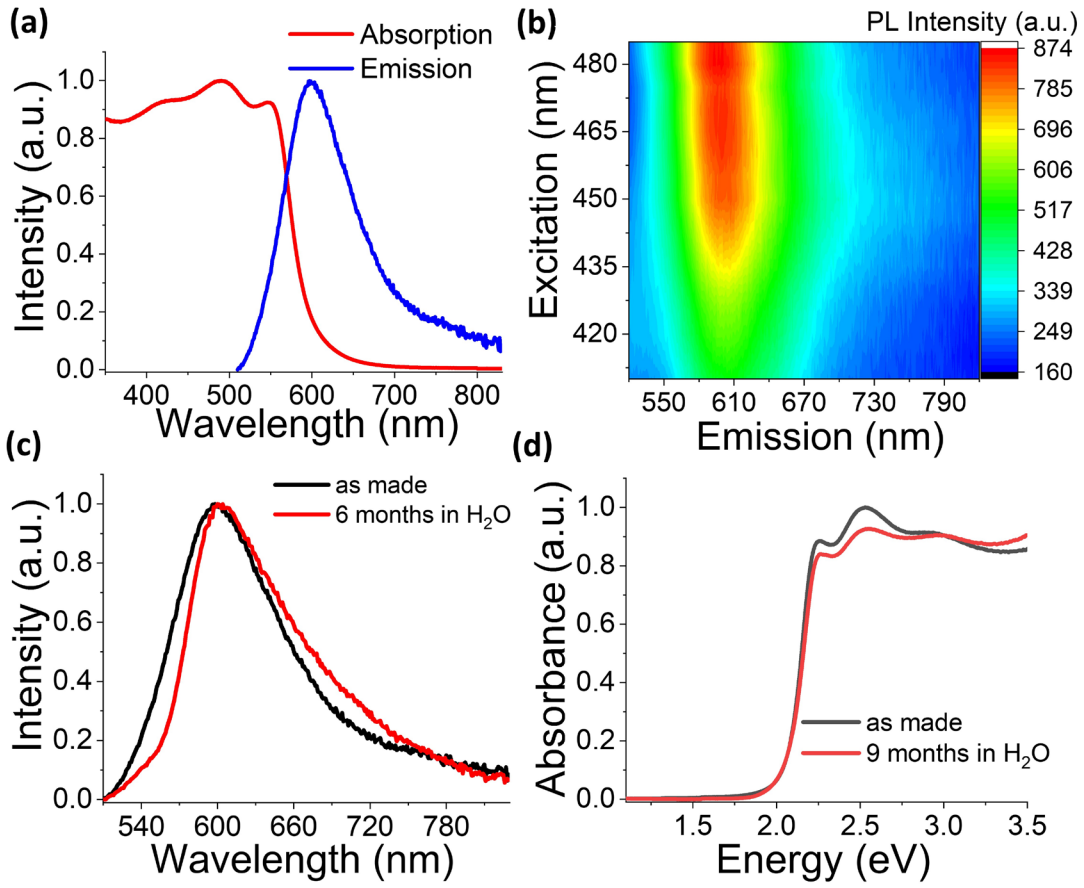

Figure 7. a) The recorded absorption and emission spectra of (DHS)Bi_2I_8 compound at RT, b) PLE spectra map of the pristine material at RT, c, d) Comparison of PL and absorbance spectra for the fresh sample and the H_2O treated one.

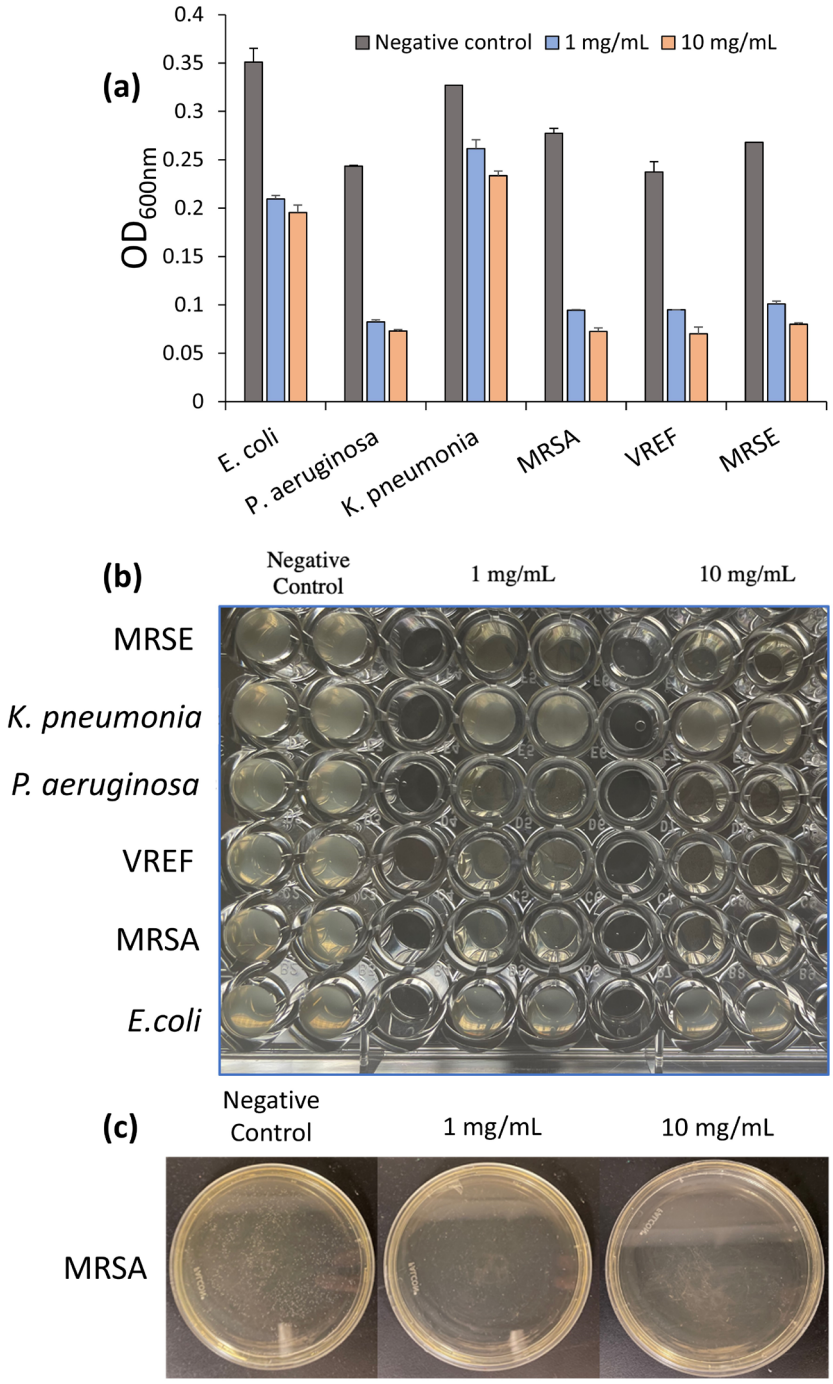

Figure 8. Antibacterial activity study of (DHS)Bi_2I_8. a), OD_{600nm} value was measured to show the activity of material against Gram-negative bacteria (*E. coli*, *K. pneumonia*, and *P. aeruginosa*) and Gram-positive bacteria including (MRSA, MRSE and VREF). b) Snapshot of antibacterial activity in 96-well plate. c) Pictures of MRSA colonies incubated by 10^{-4} dilution for 12 h.

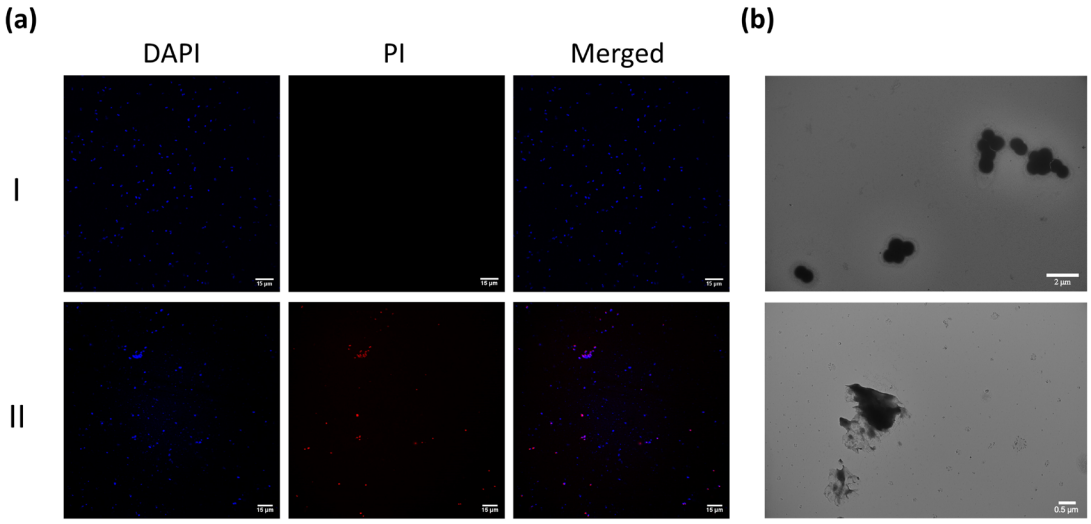

Figure 9. Membrane disruption study of (DHS)Bi_2I_8. a) fluorescence images of MRSA with no treatment (I) and with (DHS)Bi_2I_8 treatment (II). b) TEM images of untreated MRSA (above) and treated cell (bottom). The result clearly demonstrates the rupture of the cell membrane upon treatment with (DHS)Bi_2I_8.

Table 1. Crystal and structure refinement data for (DHS)Bi_2I_8 at 296 K.

Crystal system	monoclinic
Space group	$P2_1/c$
Unit cell dimensions	a = 13.058(3) Å, α = 90° b = 22.069(6) Å, β = 90.020(4)° c = 14.106(4) Å, γ = 90°
Volume	4065.1(18) $Å^3$
Z	4
Density (calculated)	2.971 g/cm^3
Independent reflections	8330 [R_{int} = 0.0755]
Completeness to θ = 29.33°	99.9%
Data / restraints / parameters	8330 / 1254 / 571
Goodness-of-fit	1.025
Final R indices [I>2σ(I)]	R_{obs} = 0.0456, wR_{obs} = 0.0968
R indices [all data]	R_{all} = 0.0866, wR_{all} = 0.1170
Largest diff. peak and hole	1.216 and -1.484 $e \cdot Å^{-3}$

$R = \Sigma||F_o|-|F_c|| / \Sigma|F_o|$, $wR = (\Sigma[w(|F_o|^2 - |F_c|^2)^2] / \Sigma[w(|F_o|^4)])^{1/2}$ and $w=1/(\sigma^2(I)+0.0004I^2)$

Table of Contents Graphic